JMEPEG (2024) 33:372–384
https://doi.org/10.1007/s11665-023-07968-5

©ASM International
1059-9495/$19.00

TECHNICAL ARTICLE

Effect of Post-Weld Heat Treatment on Hardness and Corrosion Resistance of Dissimilar Electron Beam Welded Joints of Inconel 713LC and AISI 4140 Steel

G. Baxevanis, F. Siokos, A. Kaldellis, D. Ioannidou, V. Stergiou, P. Skarvelis, and P.E. Tsakiridis

Submitted: 29 October 2022 / Revised: 30 January 2023 / Accepted: 31 January 2023 / Published online: 22 February 2023

Dissimilar welding of Inconel 713LC superalloy and high strength AISI 4140 steel was conducted using Electron Beam (EB) welding process. The present research study focuses on the effect of post-weld heat treatment (PWHT) on the produced dissimilar joints' microstructure, mechanical properties and corrosion behavior assessment. PWHT was accomplished at 650°C for 2, 4 and 6 h, following air cooling. The microstructure study was carried out by light optical (LOM) and scanning electron microscopy (SEM), coupled with energy-dispersive spectroscopy (EDS) analysis. The mechanical behavior of the EB joints was investigated via Vickers hardness testing. For the assessment of the EB joints' corrosion resistance, potentiodynamic polarization tests were performed in 3.5 wt.% NaCl solution, at various temperatures. The corrosion products evaluation was carried out by both x-ray Diffraction (XRD) and scanning electron microscopy (SEM). PWHT leds to the microstructure modification of both Inconel 713LC and AISI 4140 in the dissimilar welding zones. The heat treatment holding time increment resulted in the development of more uniform mechanical response among base metals and fusion/heat affected zones, whereas corrosion resistance became progressively weaker.

Keywords corrosion, electron beam welding, microstructure, microalloyed steel, Ni-based superalloy, post-weld heat treatment

1. Introduction

The joining of dissimilar materials has progressed significantly in the recent past owing to their accrued demand in aerospace, nuclear, chemical and thermal power plants. The variable applications of the dissimilar joints are directed by the in-service requirement, wherein the involvement of each material is localized for the optimal utilization of their properties, the economic feasibility of the materials and ease of fabrication (Ref 1, 2).

Dissimilar welding exhibits significant advantages in the case of turbocharger, a structure that consists of a turbine and a compressor, both mounted onto a common shaft. Waste energy from the exhaust turns the turbine, causing the impeller to provide compressed air to the engine. Turbocharger can be used in both gasoline and diesel engines for increasing the overall efficiency, as the turbocharger delivers horsepower through an output shaft, using almost all the exhaust energy. The materials needed for the construction of the turbocharger should present high tensile and fatigue strength, good hardenability, high level of creep resistance and ductility, both because of the extreme temperature working conditions and the applied critical mechanical stresses (centrifugal, torsional and bending forces development) (Ref 3-5).

The turbocompressor rotor can be manufactured with combinations of dissimilar materials in order to improve mechanical performance and decrease the cost of production. Its construction can be based on the dissimilar welding of a Ni-based superalloy impeller, with a shaft made from a quench & tempered microalloyed steel, in order to combine their excellent performance under high temperature (Ref 6). Nevertheless, their fusion is a very difficult task, due to the significant difference in chemical composition and mechanical properties of these two types of materials, which can lead to the formation of solidification internal cracks, porosity, inclusions and microstructural segregation. On the other hand, those defects could be relatively faced through post-weld heat treatment (PWHT), which could be beneficial in improving both joint strength and fracture toughness.

Although there is a lot of work regarding nickel-based superalloys and stainless steels dissimilar welding studies (Ref 7, 8), the research carried out in the field of dissimilar welding between nickel-based superalloys and microalloyed steels is relatively limited (Ref 4, 5), especially in case of Electron Beam welding (EBW). A similar type of joint between Inconel 713LC and AISI 4140 steel could be used in various industrial high-temperature applications, such as aerospace, power plants, automotive, marine, petrochemical plants, etc.

EBW produces high-quality joints, as during the welding process high energy density ($\approx 10^6$ W/cm^2) is developed (Ref 9, 10) and it is often used for advanced materials and complex, critical parts such as turbine rotors. It is carried out in a high

G. Baxevanis, F. Siokos, A. Kaldellis, D. Ioannidou, and **P.E. Tsakiridis**, Laboratory of Physical Metallurgy, School of Mining and Metallurgical Engineering, National Technical University of Athens, Athens, Greece; and **V. Stergiou** and **P. Skarvelis**, Special Processes and Materials Technology Department, Hellenic Aerospace Industry, Schimatari, Greece. Contact e-mail: ptsakiri@central.ntua.gr.

vacuum chamber, thus producing high-quality joints because of the very low rate of oxidation (Ref 11). Also, it intensifies the degassing process occurring during the phases' melting. When a beam power density above 10^5 W/cm^2 is obtained, a deep welding effect is observed (keyhole), enabling to weld thick-walled parts in a single pass, which in the case of steel can reach a thickness of 200 mm. It allows deep penetration and creates homogeneous, narrow V-shaped welds, with small heat-affected zones (HAZ), due to high cooling rates. It should be noticed that in the case of dissimilar welding, the small weld bead size of EB welds minimizes the mixing of dissimilar metals, thus minimizing the limits of the brittle zones arising from the base metals' chemical variation (Ref 12, 13).

AISI 4140 is a medium carbon microalloyed steel that mainly contains Mn, Cr and Mo. Due to its high strength and toughness, good fatigue behavior and machinability, the alloy is widely used in important structural components such as generator spindle, crane weight-on-wheel, automotive crankshafts, oil drill pipe joints of deep well, armor materials and other applications (Ref 14, 15).

lnconel 713LC is a high strength nickel-chromium alloy that is utilized for jet engine gas turbine blades. It presents excellent resistance to thermal fatigue and good castability while offering high rupture strength in the temperature range of 930°C. Its good weldability characteristics are associated with the sluggish precipitation kinetics of the primary strengthening body-centered tetragonal Ni_3Nb, γ" phase (Ref 16, 17). This sluggish age-hardening response results in relatively low strength, and high ductility heat affected zone (HAZ) during the initial aging treatment, permitting relaxation of residual stresses and hence leading to a reduction in strain-age cracking tendency (Ref 18, 19). During solidification that occurs while welding with fusion methods, in addition to primary γ-dendrites, eutectic phases such as NbC and Laves [$(Ni, Cr, Fe)_2$ (Nb, Mo, Ti)] are also formed. More specifically, the brittle intermetallic Laves phases is formed according to the eutectic reaction "$L \rightarrow \gamma + Laves$" that occurs at the eutectic temperature of 1198°C. Various researchers have mentioned that the most important cause of failure and crack initiation under mechanical stresses is the evolution of those laves eutectic phases in the weld zone (Ref 20-22).

Furthermore, the observed inhomogeneity in the microstructure and, as a result, in the mechanical properties along the dissimilar welded joints is a serious issue that is mainly governed by the chemical composition of the metals and the heat input. During the welding process, AISI 4140 steel in Q&T condition does not anymore consists of tempered martensite in the HAZ, as needle-like martensite is nucleated and grows as a result of the fast austenitization near the fusion zone (FZ). The consequent rapid cooling rate is a fact that impairs the HAZ mechanical properties, especially ductility and toughness. On the other hand, Inconel 713LC, except for the above mentioned issues with Laves formation, also presents chemical segregation issues in the FZ, due to the different composition of the alloys' joint, where secondary phases, such as carbides, nitrides and Laves can be formed and deteriorate the properties of the weld (Ref 23-25).

Consequently, post weld heat treatment (PWHT) is recommended for dissimilar joints of nickel-based superalloys with microalloyed steels, in order to improve the metallurgical structure and/or properties, reduce the steel HAZ hardness, decrease welding distortion and relieve residual stress (Ref 26). One-stage post weld heat treatment could lead not only the stress relief and the precipitation of the gamma and double prime, thus enhancing the mechanical response of 713LC, but also to the simultaneously tempering of steel, thus decreasing its hardness and generally improving the uniform mechanical response of the joint. It could also lead to the decrement of the segregation phenomena of alloying elements (Nb, Mo) on the FZ, thus avoiding the formation of brittle phases, such as Laves, carbides or nitrides.

The present investigation focuses on the dissimilar EBW between a cast Inconel 713LC turbocharger impeller and an AISI 4140 shaft, thus combining the high mechanical strength, impact toughness, creep and oxidation resistance of the former with the high fatigue strength, fracture toughness and lower cost of the latter. Furthermore, the investigation of the optimized implementation of post-weld heat treatment was carried out to enhance the microstructure-properties relationship. Finally, the dissimilar joints' corrosion resistance was also evaluated through potentiodynamic polarization.

2. Experimental

2.1 Materials and Welding Procedure

Dissimilar joints of Inconel 713LC to AISI 4140 (German Grade: 42CrMo4) low alloy steel were carried out via electron beam welding. The chemical composition of both materials is given in Table 1. Composition of Inconel 713LC was given by the manufacturer of the impeller.

The cast Inconel 713LC turbocharger impeller and the quench & tempered AISI 4140 shaft, with a diameter of 36 mm were jointed through butt welding (Fig. 1). The joint should be able to withstand temperature variations and centrifugal loading without experiencing significant deformation, which could alter the balance, introduce noise or reduce assembly life. In order to locate the parts radially (coaxial location), the blade disk and the turbine shaft were aligned by fitting a cylindrical protrusion, formed at the forehead of the turbine shaft, into a fitting hole, formed in a turbine blade disk.

The dissimilar bars presented a diameter of 36 mm and were fused by EBW on the entire periphery.

The EBW process involved placing the shaft and the turbine wheel in the vacuum chamber and focusing the electron beam on the joint to be welded. Before welding, the end surfaces of the bars were polished using SiC sandpapers and were then cleaned with acetone to remove any grease/organic contaminations or dirt residues. The bars rotations speed was kept constant at 14.5 rpm. The weld process parameters were established based on the iterative trials and the parameters chosen for the current study are shown in Table 2.

2.2 Post-weld Heat Treatment (PWHT) Modification

The welded samples were sectioned transversely to the welding direction, using a precise Struers Accutom-2 microtome. PWHT was accomplished at 650°C for 2, 4 and 6 h, following air cooling (Fig. 2). This modification targeted in stress relief minimization, tempering of martensite of AISI 4140 HAZ, eliminating unwanted developed phases (Laves or δ) and simultaneously precipitating gamma prime (γ′) and double prime (γ″) (Ref 27, 28). PWHT was performed in an inert atmosphere, thus avoiding partial oxidation phenomena.

Table 1 Chemical composition of base metals (wt.%)

Base metal	C	Cr	Al	Mo	Nb	Ti	Si	Mn	S	P	Ni	Fe
Inconel 713LC	0.048	12.26	6.36	4.58	1.64	0.715	0.067	0.002	0.004	0.005	Balance	···
AISI 410	0.40	1.12	0.02	0.18	···	···	0.33	0.93	0.031	0.025	0.17	Balance

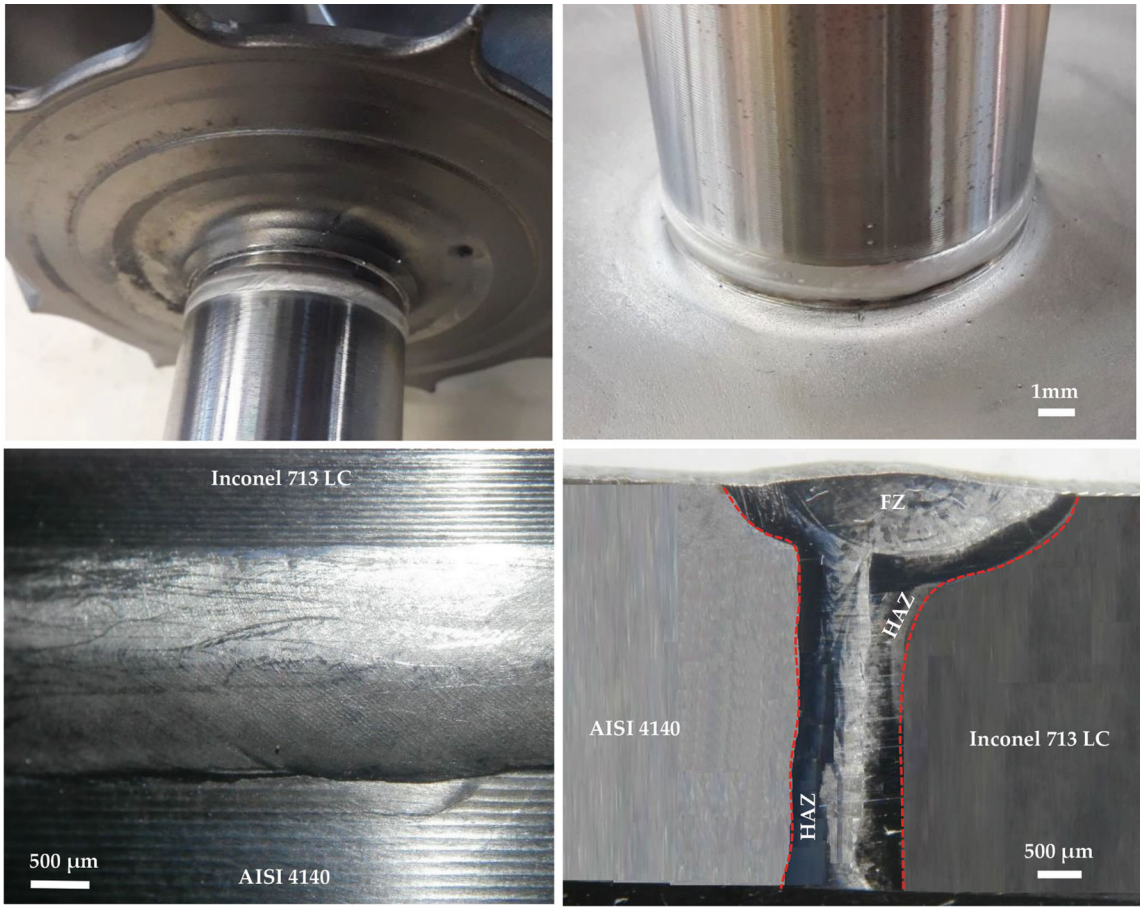

Fig. 1 Dissimilar EBW Inconel 713LC turbocharger impeller with an AISI 4140 shaft

Table 2 EBW process parameters

Process parameters	Unit	Value
Accelerating voltage	KV	50
Beam current	mA	145
Beam focus	A	3.30
Travel speed	mm/min	1640
Rotation speed	rpm	14.5
Heat input	kJ/mm	0.2656

2.3 EB Joints Characterization

The welded samples under investigation, after being impregnated in a low viscosity epoxy resin, in 30 mm diameter cylindric mold under vacuum, were cut via micro-saw and then ground and polished down to 1 μm diamond past on a lapping disk, according to conventional metallographic preparation procedures.

The polished specimens were chemically etched through two different solutions to reveal the microstructure. Specifically, AISI 4140 was etched in a Nital 2% solution and Inconel 713LC was etched locally in Kalling's No.2 solution (5 g $CuCl_2$, 100 mL ethanol, 100 mL HCl). The microstructural observation was initially carried out in an Olympus BX41M optical microscope and then, with a Jeol 6380 LV scanning electron microscope, using both secondary and backscattered electron detectors. To determine the phases' composition of the EBW joints, microanalyses were accomplished with an Oxford INCA energy dispersive spectrometer (EDS) connected to the SEM. The identification of the precipitates was also accomplished through the use of x-ray Diffraction (Bruker D8-Focus diffractometer with nickel-filtered CuKa radiation (λ = 1.5406 Å), at 40 kV and 40 mA). To assess the mechanical properties of the dissimilar joint Vicker hardness testing

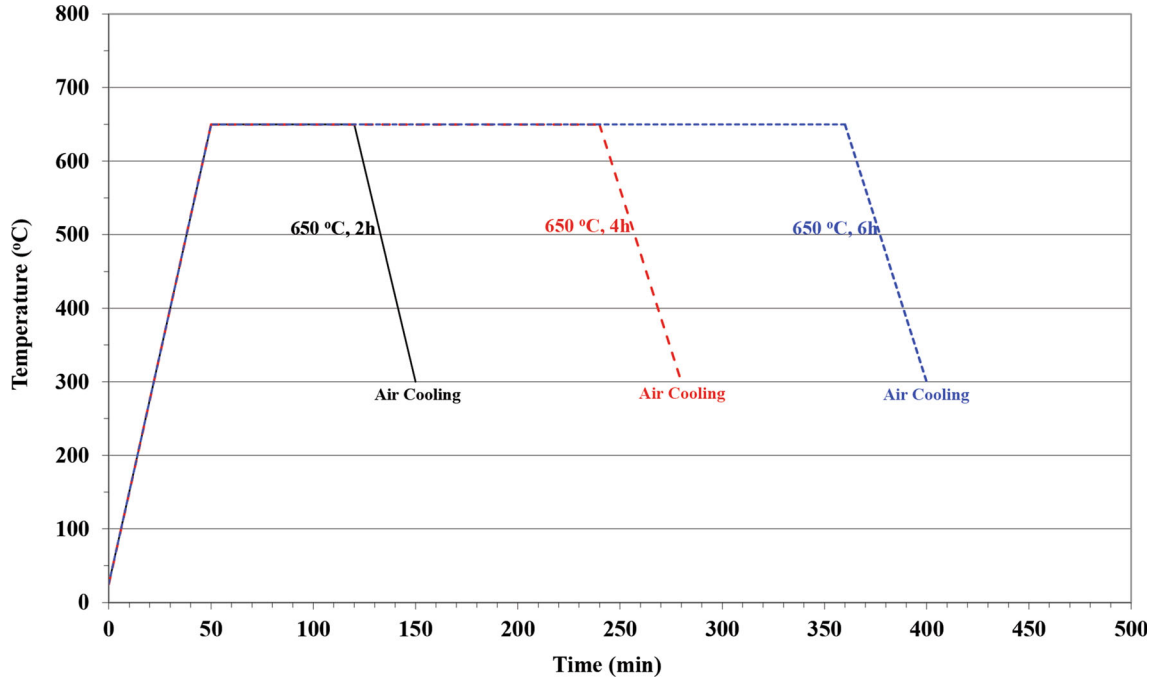

Fig. 2 PWHT at 650°C for 2, 4 and 6 h, following air cooling

was conducted using an HV-50Z hardness tester, implementing 196N for 15 s. The EB fusion zone, the heat-affected zone and base metals were covered during the hardness test, and then correlated with the microstructural observations.

2.4 EB Joints Potentiodynamic Corrosion Tests

To evaluate the corrosion behavior of the EB joints, potentiodynamic corrosion tests were performed in an electrolyte of 3.5 wt.% NaCl, at 25, 50 and 80°C (± 2°C). The solution was prepared by using distilled water and analytical grade NaCl. The selected samples—extracted from the EB zone—as the working electrode, a saturated calomel electrode (SCE) as the reference electrode, and graphite as the counter electrodes were combined in a conventional three-electrode cell. The experiments were conducted in accordance with ASTM G5 (Ref 29), using an Amel Potentiostat/Galvanostat Model 2551, with VApeak software. An open circuit potential was established within 15 min, before the electrochemical tests. After that, a polarization test was performed at a scanning rate of 0.1 mV/s from − 250 to + 1600 mV. The produced potentiodynamic curves were used to designate the corrosion potential, corrosion current density and the slope of the anodic and cathode curve of the tested materials.

The phase identification of the corrosion products was carried out using a Bruker D8-Focus diffractometer with nickel-filtered CuKa radiation (λ = 1.5406 Å), at 40 kV and 40 mA. SEM analysis was also used in order to detect the morphology and the composition of the developed corrosion products, on the surface of the corroded samples.

3. Results and Discussion

Single pass EB welding was used to join the Inconel 713LC superalloy and AISI 4140 steel. The weld samples were shown in Fig. 1. The observed surfaces were free of solidification or liquation cracks and porosity. The maximum width of HAZ was detected near the surface, whereas was decreased in relation with the weld depth, as the heat input to the weld surface decreased along the weld depth.

Characteristic micrographs of the as-welded, EBW fusion zone, along with the heat-affected zones and the corresponding base metals, obtained through optical and scanning electron microscope in polished sections, are presented in Fig. 3. Regarding the microstructural features of Inconel 713LC base metal (BM), coarse grains of the gamma austenitic matrix with the presence of twins were observed. Borides and carbides rich in Nb were also detected dispersed in the austenitic matrix. Most of the precipitates were observed at the fusion boundary of Inconel 713LC alloy and weld zone. During the temperature increment, the nickel-based superalloy is partially melted and interacted with the weld fusion zone, leading to interdiffusion phenomena and the development of various precipitates.

Mixed (Ti,Nb)C carbides were identified both in the base metal and HAZ, especially in grain boundaries, with the form of a continuous film. The initial grain boundary phases were not fully dissolved into the austenitic matrix during heating, leading to the formation of a low melting point eutectic and melting of the grain boundary region.

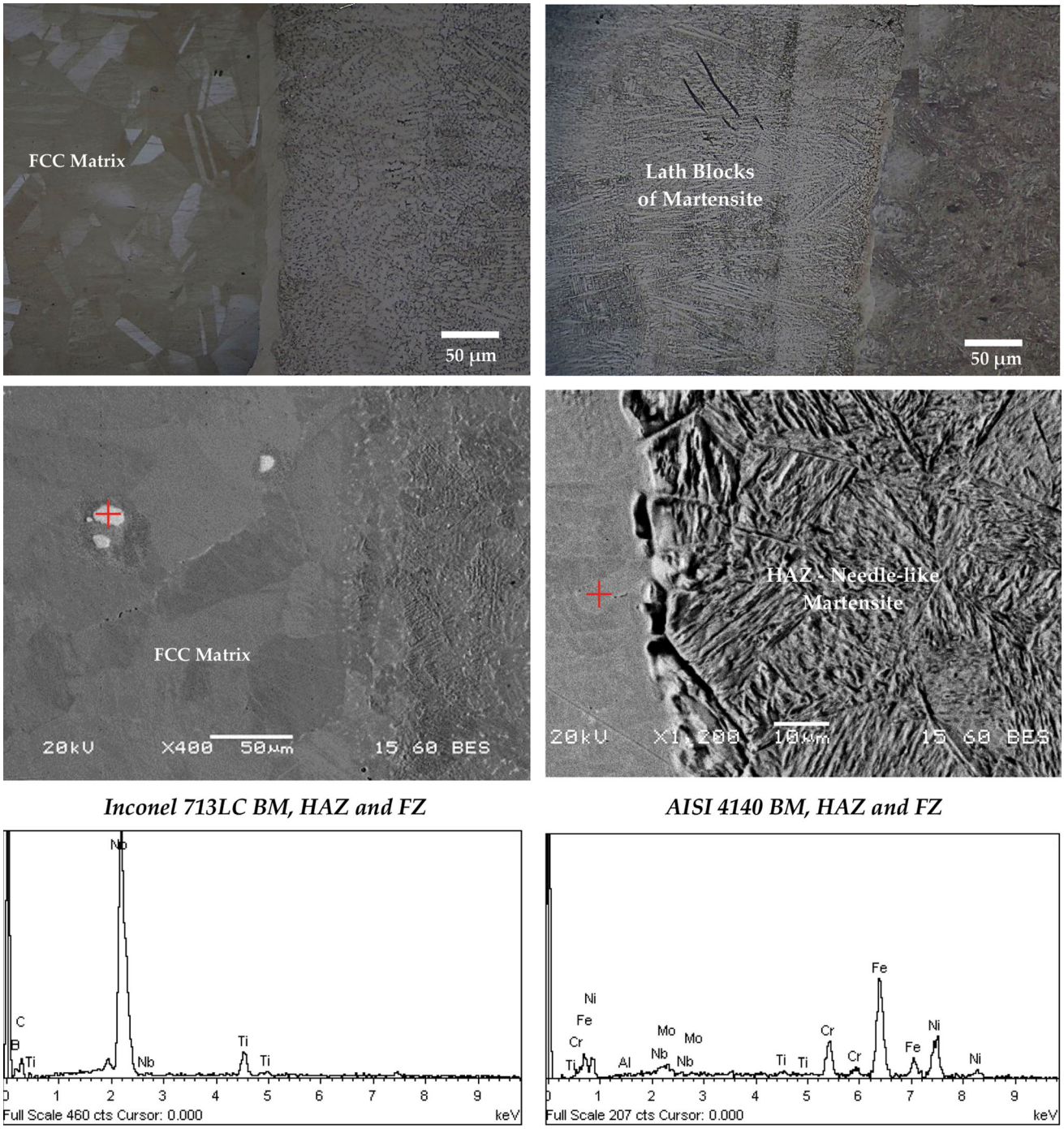

Fig. 3 Representative micrographs, under OM and SEM, in conjunction with EDS analyses of Inconel 713LC and AISI 4140 dissimilar welding zones (BM, HAZ and FZ)

Finally, larger precipitates, with cuboidal or parallelepipedal form, with a side length in the range of 10-20 μm, were also observed near the FZ, with a composition similar to Laves phase, a hexagonally close-packed phase that is generally accepted to be of the form $(Ni, Cr, Fe)_2(Nb,Mo,Ti)$.

On the other hand, although the microstructure of AISI 4140 base metal mainly consists of tempered martensite in the form of the lath blocks (packets and prior austenite grain boundaries) in the HAZ due to rapid cooling, martensitic modification has been carried out leading to the development of the needle-like structure.

FZ has been developed with the form of mixed dendritic structure, consisting of columnar or elongated and equiaxed sub-structures, highly enriched in Ni, Fe and Cr, perpendicular to the beam direction, whereas some solidification lines were also observed (Fig. 4). The microstructural observations do not identify any defects or the solidification cracks either in the fusion zone or in the HAZ region.

Except for the main dendrite structure, finer irregular-shaped particles of similar composition with the corresponding Laves phases observed in the HAZ, were also identified in the interdendritic solidifying regions. The development of Laves

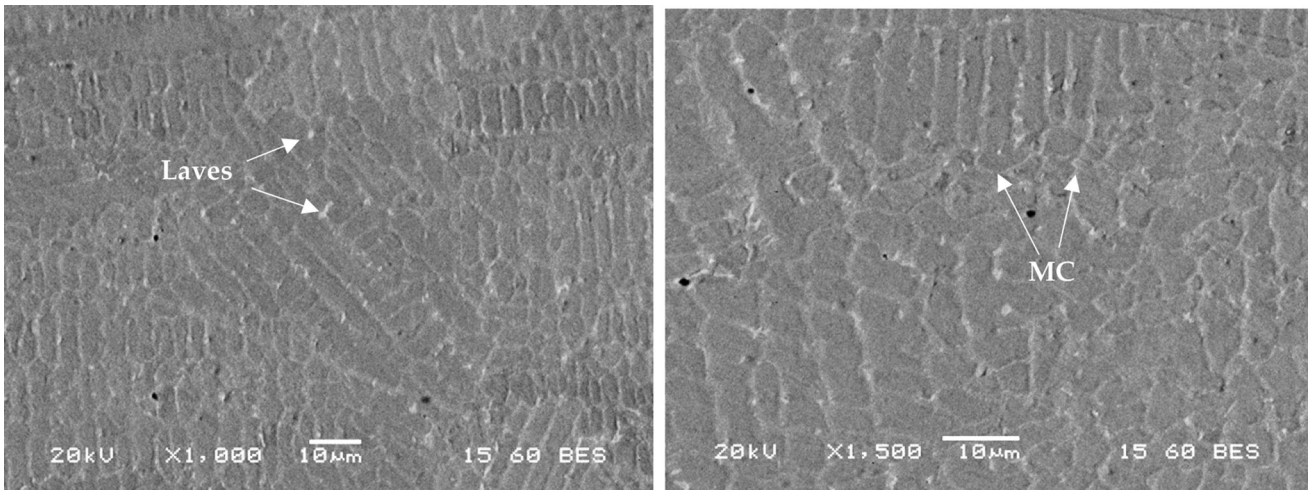

Fig. 4 Backscattered electron micrographs of dissimilar FZ

phases requires 10-30% of Nb. As a result, segregation, a time-dependent phenomenon is necessary for the nucleation inception of Laves phase. These remaining interdendritic Laves phases have been rapidly solidified during EBW, because of the high cooling rate and their size has been kept low, as the segregation of elements has been prevented.

As was mentioned above, it is well known that the most important cause of failure and crack initiation under mechanical stresses is the evolution of those Laves eutectic phases in the weld zone. Furthermore, regarding the HAZ of AISI 4140 steel, after the welding process did not anymore consist of tempered martensite, as need-like structures were nucleated and grown due to the fast austenitization and the consequent rapid cooling, thus decreasing ductility and toughness. Consequently, one stage PWHT was applied at different times to improve the metallurgical structure and/or properties, reduce the steel HAZ hardness, decrease welding distortion, and relieve residual stress.

The microstructural characteristics of the EB fusion zone, along with the corresponding heat-affected zone and the base metals are presented in Fig. 5. According to the results, implementing the post-weld heat treatment and increasing the holding time, the needle-like martensite changed progressively to plate morphology. The coarse and interconnected Laves particles, precipitated in the HAZ, have progressively dissolved and their size has been significantly diminished. Moreover, due to the Laves phases dissolution MC carbides, rich in Nb, evolved both inside the grains and the grain boundaries.

Concerning the FZ, the PWHT modification at 650°C did not affect its columnar dendritic structure (Fig. 6).

The fine dendritic structure has been developed with well-separated interdendritic regions with lower Nb concentration, a fact that led not only to the formation of finer and discrete Laves phase, but also to the partial dissolution of Nb into the matrix and to the consequent development of precipitates rich in Nb (γ” and carbides). The Laves phase size minimization at the grain boundaries of the inter-dendritic regions was beneficial for reducing embrittlement phenomena and for improving the ductility and strength of the FZ.

The above observations were also confirmed by the results of the fusion zone x-ray Diffraction patterns analysis, presented in Fig. 7. Except for mixed (Ti,Nb)C and NbC carbides, other carbides such as M_6C, $M_{23}C_6$ were also identified in the fusion zone regardless of the heat treatment. The peaks in the case of MC type carbides seem to be strengthened, especially in the case of PWHT for 6 h, simultaneously with the corresponding decrement of those of Laves phases. The greater the duration of the PWHT, the higher the decomposition of the laves phases, a fact that led to Nb dissolution in the interdendritic regions and to the consequent formation of another type of precipitates (carbides and γ”).

The hardness profile of the EB joint, along with the corresponding base metals, carried out at a depth zone of 4 mm on either side, is presented Fig. 8. The peak hardness of 530 HV was identified at the HAZ of AISI 4140 steel, in the as-welded sample. Due to the heating and cooling cycle under the welding process, as mentioned earlier, the tempered martensite in the HAZ changed morphology to needle-like martensite. As the PWHT time increased the hardness of the HAZ got normalized due to tempering of needle-like structures. This led to morphologies of prior austenite grains, divided into several packets which consist of parallel blocks composed of laths arranged parallel to each other. On the other hand, in the case of Inconel 713LC, the PWHT led to increased hardness, both in BM and HAZ. The increase in hardness, especially after 4 and 6 h, was attributed to the partial decomposition of brittle Laves phases and the volume fraction increment of the main strengthening phases γ′ and γ″, as well as of the secondary carbides rich in Nb. The hardness rise has been usually observed in the very early stage of ageing (approximately 60% increase over the first 4 min at 760°C) (Ref 30), while that increment has been mainly attributed to the development of spherical γ′ precipitates (after a step of ageing for 4 h at 680°C) (Ref 31).

Figures 9 and 10 present the comparative diagrams of the potentiodynamic polarization tests, carried out in an electrolyte of 3.5 wt.% NaCl, at 25 and 80°C (± 2°C) in EB joints, before and after PWHT, at 2, 4 and 6 h.

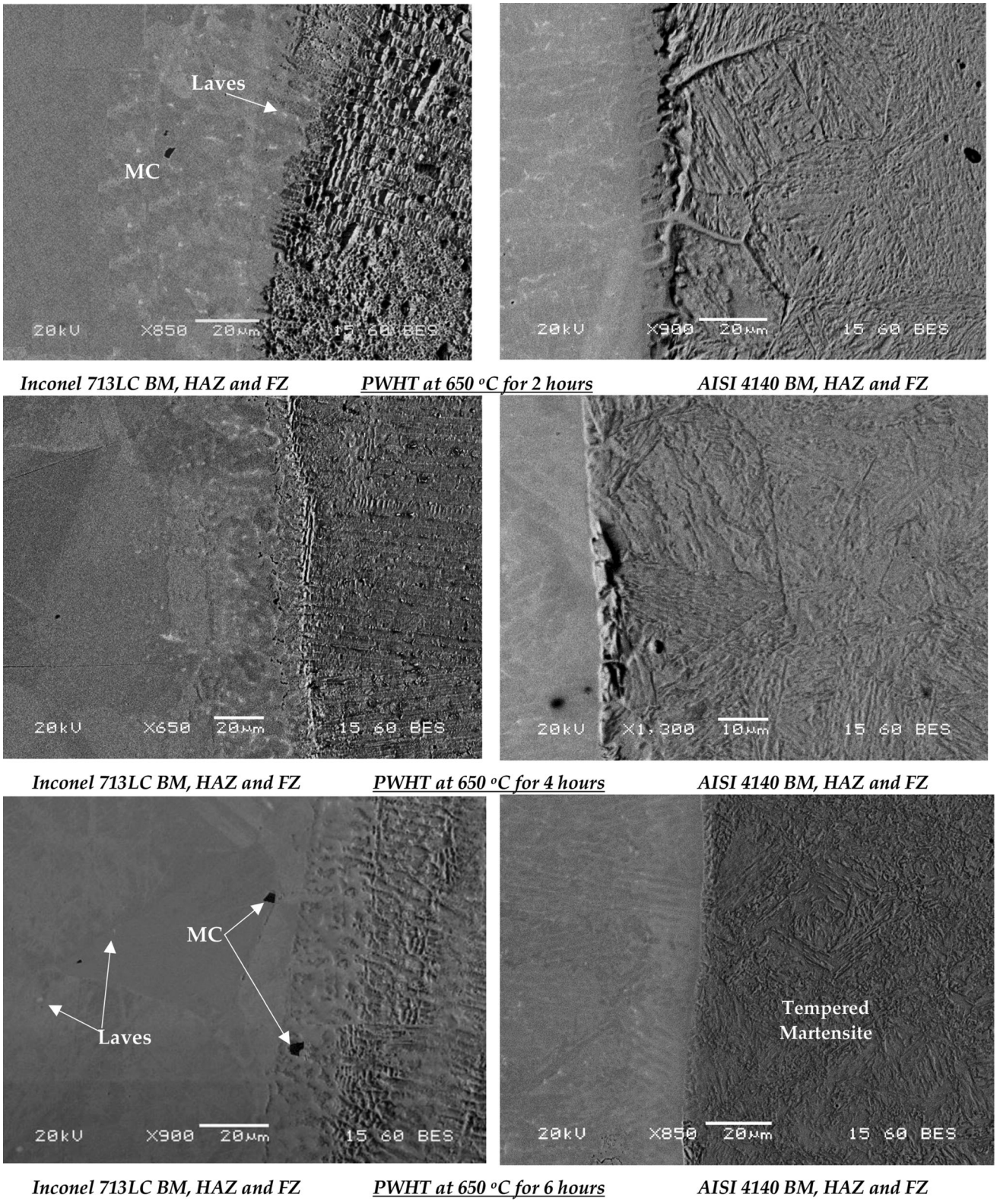

Fig. 5 Representative micrographs of Inconel 713LC and AISI 4140 dissimilar welding zones (FZ, HAZ and BM), after PWHT at 650°C for 2, 4, and 6 h

According to the results, the increase in PWHT holding time led to a lower Open Circuit Potential (OCP). Furthermore, as the immersion temperature increased, the I_{corr} in all cases was gradually increased, indicating that the corrosion rate also increased, since the temperature is the driving force for ion diffusion, and the corrosion rate accelerated with the temperature rise. That weaker corrosion behaviour of PWHT samples should be attributed both to tempering results on AISI 4140

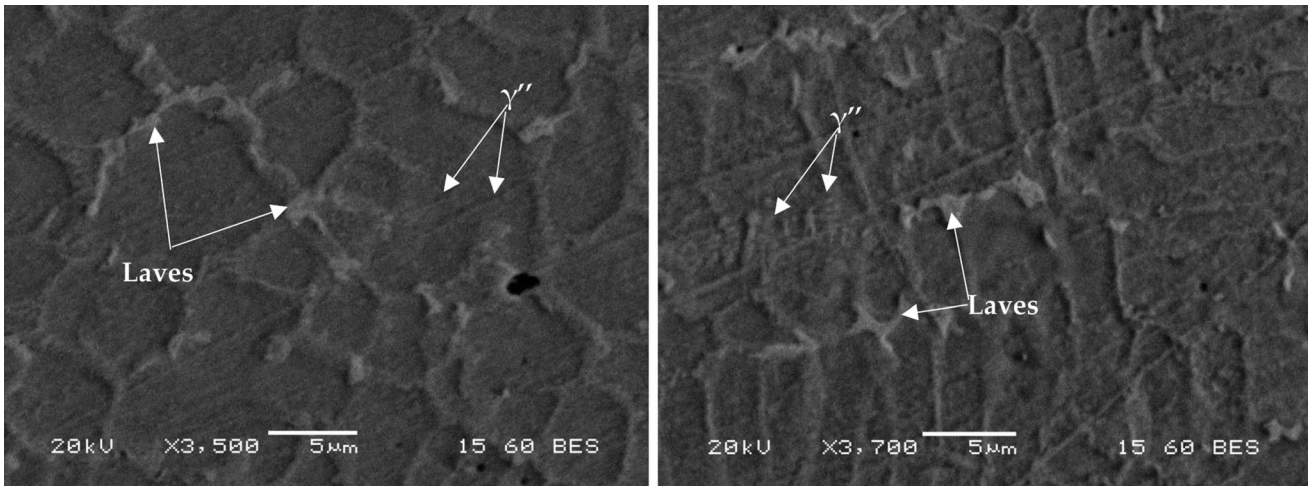

Fig. 6 Backscattered electron micrographs of FZ after PWHT at 650°C for 6 h

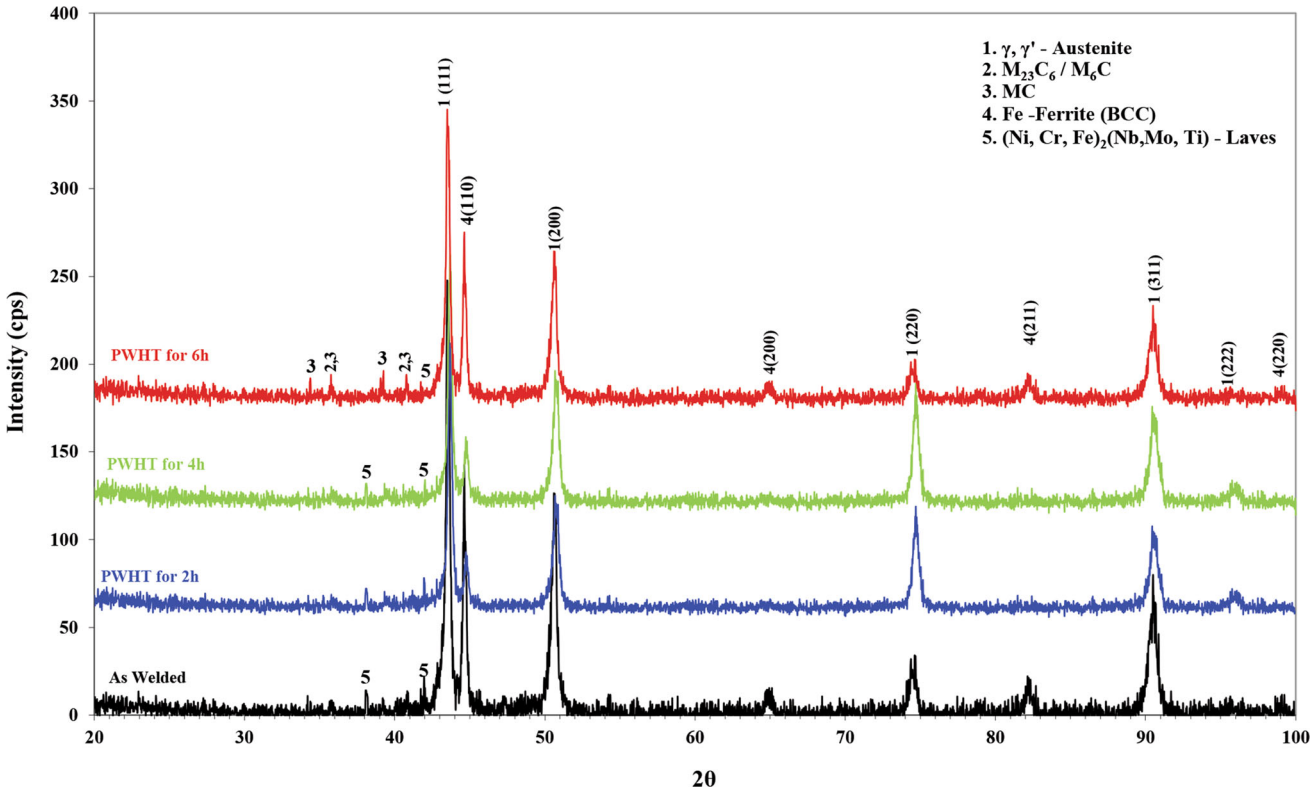

Fig. 7 XRD patterns of the dissimilar FZ with and without PWHT

steel microstructure (segregation of carbon, carbides precipitation, etc.) and the precipitation phenomena on Inconel 713LC (fine precipitation of γ′, γ″ and carbides, especially in HAZ).

Comparing the mechanical behavior with the corresponding corrosion response of the as-welded and PWHT samples, it should be mentioned that the better the hardness assessment, the weaker the corrosion resistance. This general behavior should be attributed to the abovementioned phenomena, which present an advert effect on mechanical properties and corrosion resistance. Secondary precipitates of both alloys, γ′ and γ″ in Inconel 713LC and stable and metastable carbides in AISI 4140, by carbon segregation to lattice defects, such as cementite and epsilon carbide, can improve the uniform mechanical response of the dissimilar welding by the increase of hardness of Inconel 713LC and the corresponding decrease on AISI 4140 steel. However, the presence of the above secondary precipitates impairs the corrosion resistance of both alloys.

The corrosion products composition and morphology developed during potentiodynamic polarization on EBW surface in

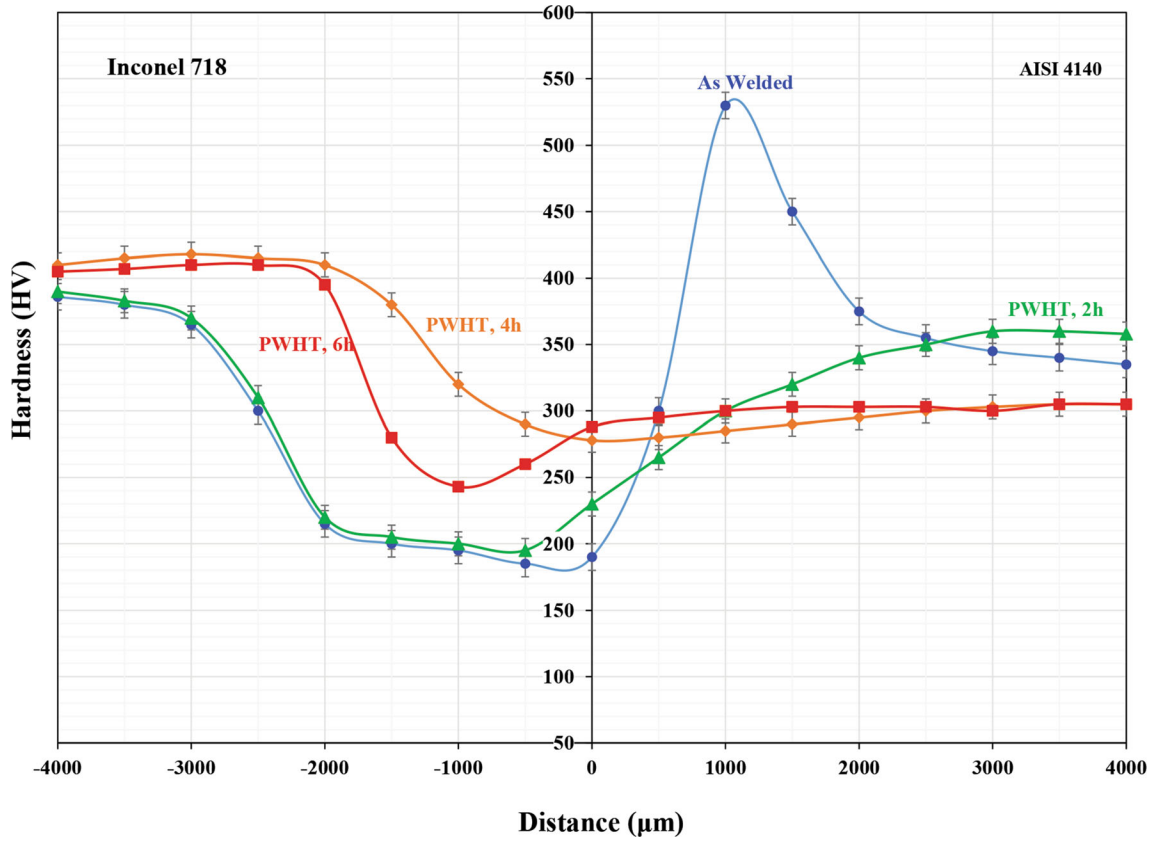

Fig. 8 Base metals and EBW hardness with and without PWHT

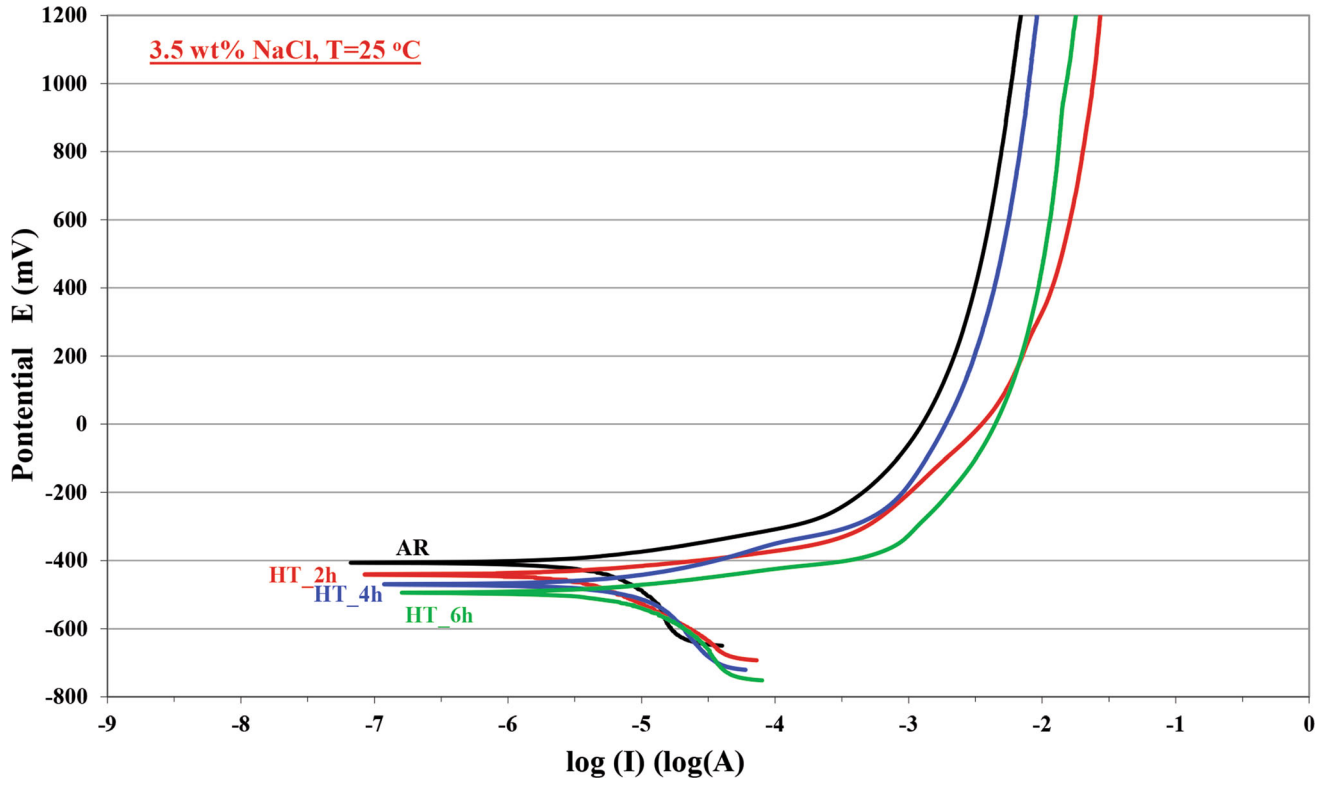

Fig. 9 EB joints potentiodynamic polarization curves in 3.5 wt.% NaCl at 25°C

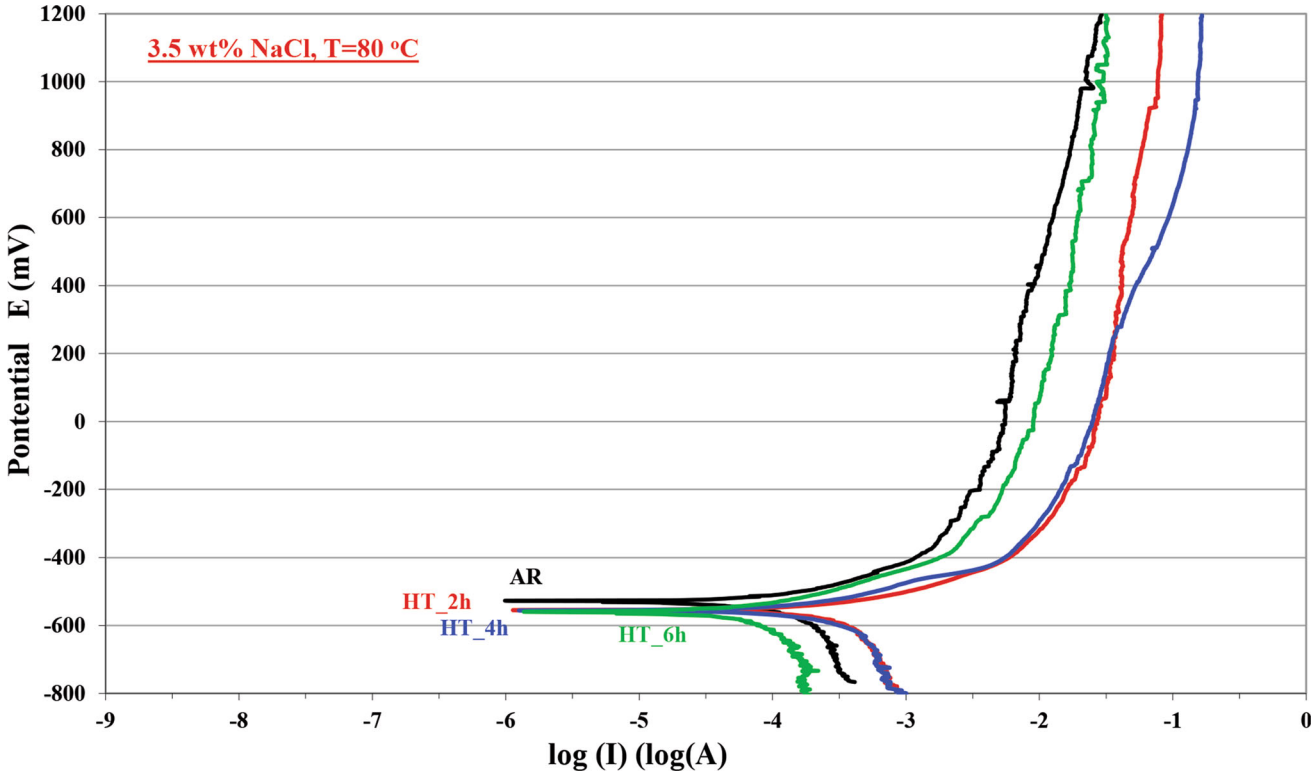

Fig. 10 EB joints potentiodynamic polarization curves in 3.5 wt.% NaCl at 80°C

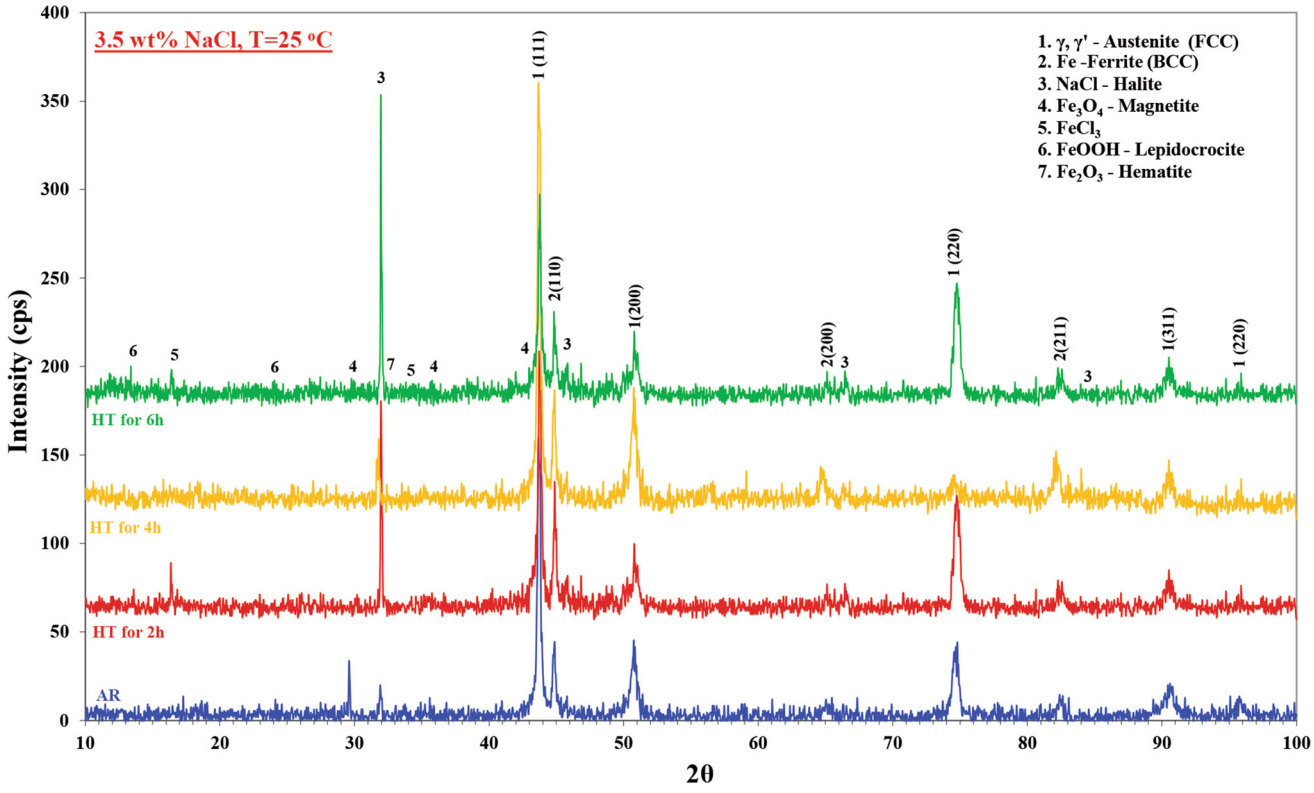

Fig. 11 Comparative XRD patterns of corroded samples in 3.5 wt.% NaCl aqueous at 25°C

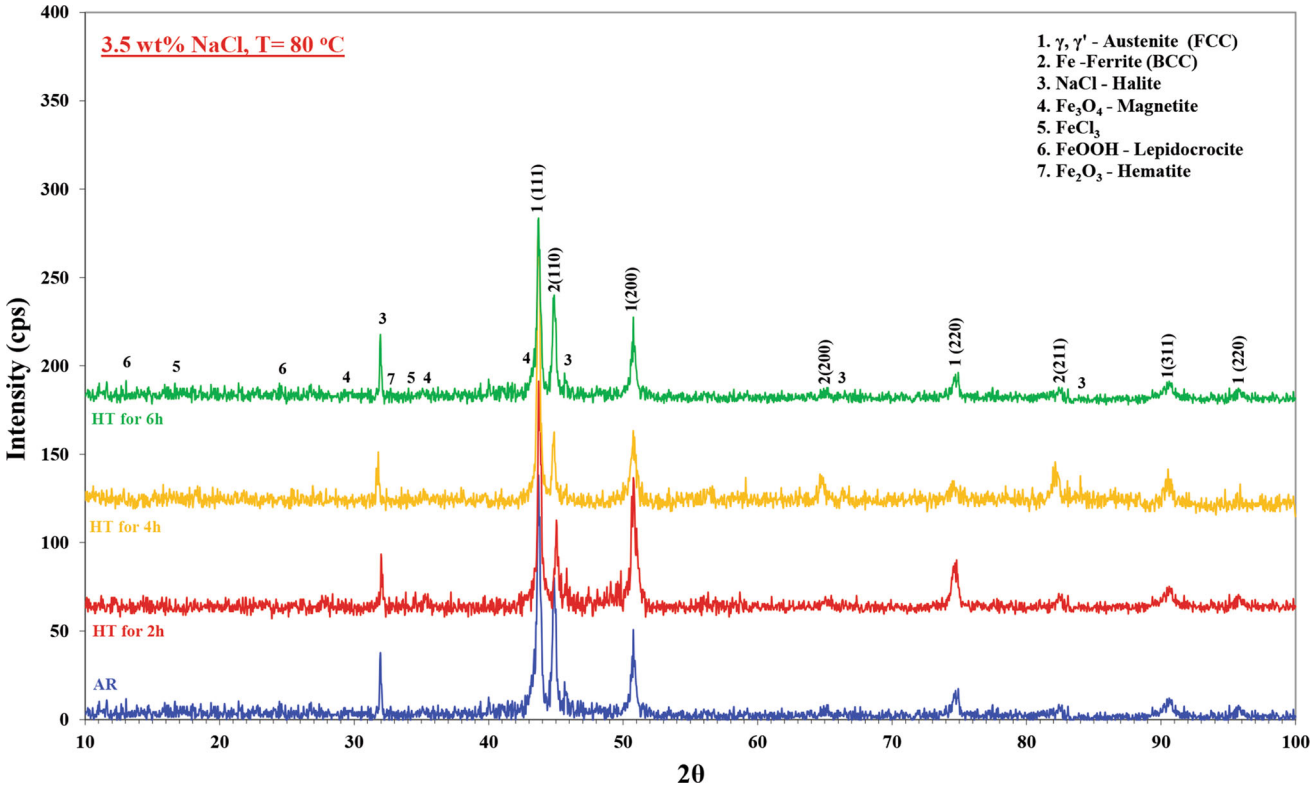

Fig. 12 Comparative XRD patterns of corroded samples in 3.5 wt.% NaCl aqueous at 80°C

3.5 wt.% NaCl, at 25°C and 80°C, were investigated via x-ray diffraction (Figs. 11 and 12) and scanning electron microscopy, respectively (Fig. 13). Regarding the XRD results of the corroded samples the main products in all cases were mainly related to the stable and unstable ferrous oxides and hydroxides, indicating that AISI 4140 steel was mainly corroded, whereas Inconel 713LC was barely attacked during corrosion testing. Regarding AISI 4140 steel, its corrosion products were a mixture of lepidocrocite (γ-FeOOH) magnetite (Fe_3O_4), and hematite (α-Fe_2O_3). The composition of corrosion products did not alter significantly due to temperature variations.

The distribution of the corrosion product in the AISI 4140 steel HAZ-FZ interface was also investigated by SEM. The main corrosion products originated from AISI 4140 steel. In the presence of chloride ions, the produced ferrous hydroxide reacted with chloride first to produce unstable hydrochloride and then was further oxidized into FeOOH as an intermediate transition product. Magnetite (Fe_3O_4) was detected in the form of large-sized agglomerates, while needle-like or rod-like aggregate morphologies rich in chloride ions were identified as lepidocrocite (γ-FeOOH). On the other hand, the FZ rich in chromium and nickel seemed to suffer less. In the case of exposing the FZ at higher temperature, the morphology of pitting cavities (Fig. 13d) was observed in areas rich in Nb, indicating the presence of secondary precipitates, which were partially removed. However, the nickel solid solution in the FZ, with about 35 wt.% of nickel and 15 wt.% of chromium, presented higher resistance and suffered less from dealloying.

4. Conclusions

In the present research study, the dissimilar welding between Inconel 713LC and microalloyed AISI 4140 steel by EB method, as well as the influence of the post-weld heat treatment modification on the microstructure-properties relationship were investigated. Post-weld heat treatment modification at 650°C resulted in a more uniform mechanical response with increasing the holding time, whereas corrosion resistance became progressively weaker. PWHT led to the improvement of both Inconel 713LC hardness, via γ′ and γ″ nucleation and growth and the microstructure of AISI 4140 via tempering effects and modification of needle-like martensite in the HAZ to lath morphology. On the other hand, the increase of PWHT holding time led to a lower OCP and higher I_{corr} values, indicating that the corrosion resistance decreased. The greater the duration of the PWHT, the higher the corrosion rate, since the presence of the above secondary precipitates, γ′ and γ″ in Inconel 713LC and stable and metastable carbides in AISI 4140, impaired the corrosion resistance of both alloys.

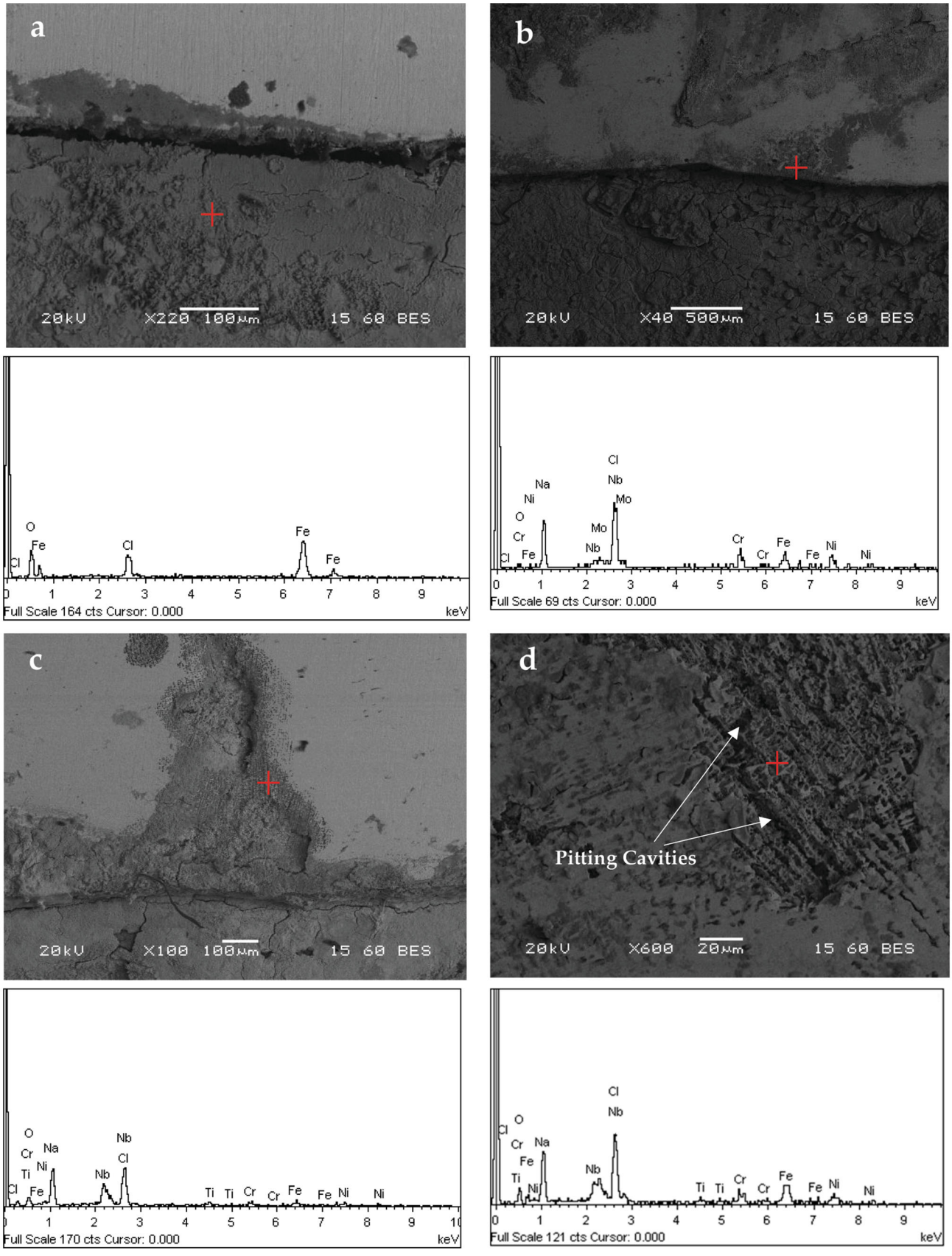

Fig. 13 Micrographs and EDS analyses of corroded samples in the AISI 4140 HAZ-FZ interface. (a) As-Welded, 25°C (b), As-Welded, 80°C (c) PWHT for 6 h, 25°C, and (d) PWHT for 6 h, 80°C

References

1. Y. Fang, X. Jiang, D. Mo, D. Zhu and Z. Luo, A Review on Dissimilar Metals' Welding Methods and Mechanisms with Interlayer, *J. Adv. Manuf. Technol.*, 2019, **102**, p 2845–2863.
2. T. Patterson, J. Hochanadel, S. Sutton, B. Panton and J. Lippold, A Review of High Energy Density Beam Processes for Welding and Additive Manufacturing Applications, *Weld World*, 2021, **65**, p 1235–1306.
3. M.M. Mohaideen, Optimization and Analysis on Turbine Rotor of a Turbo Shaft Engine, *Procedia Eng.*, 2012, **38**, p 867–871.
4. X.B. Liu, G. Yu, M. Pang, J.W. Fan, H.H. Wang and C.Y. Zheng, Dissimilar Autogenous Full Penetration Welding of Superalloy K418 and 42CrMo Steel by a High Power CW Nd:YAG Laser, *Appl. Surf. Sci.*, 2007, **253**, p 7281–7289.
5. M. Anuradha, V.C. Das, D. Venkateswarlu and M. Cheepu, Microstructure Characterization in Dissimilar Tig Welds of Inconel Alloy 713LC and High Strength Tensile Steel, *Mater. Sci. Forum*, 2019, **969**, p 496–501.
6. S.H. Baghjari and S.A.A. AkbariMousavi, Experimental Investigation on Dissimilar Pulsed Nd: YAG Laser Welding of AISI 420 Stainless Steel to Kovar Alloy, *Mater. Des.*, 2014, **57**, p 128–134.
7. A.K. Maurya, C. Pandey and R. Chhibber, Dissimilar Welding of Duplex Stainless Steel with Ni Alloys: A Review, *Int. J. Press. Vessel. Pip.*, 2021, **192**, p 104439.
8. S.A. David, J.A. Siefert and Z. Feng, Welding and Weldability of Candidate Ferritic Alloys for Future Advanced Ultrasupercritical Fossil Power Plants, *Sci. Technol. Weld. Join.*, 2013, **18**, p 631–651.
9. Z. Sun and R. Karppi, The Application of Electron Beam Welding for the Joining of Dissimilar Metals: An Overview, *J. Mater. Process. Technol.*, 1996, **59**, p 257–267.
10. C. Wiednig, C. Lochbichler, N. Enzinger, C. Beal and C. Sommitsch, Dissimilar Electron Beam Welding of Nickel Base Alloy 625 and 9% Cr Steel, *Procedia Eng.*, 2014, **86**, p 184–194.
11. M.K. Keshavarz, S. Turenne and A. Bonakdar, Solidification Behavior of Inconel 713LC Gas Turbine Blades During Electron Beam Welding, *J. Manuf. Process.*, 2018, **31**, p 232–239.
12. A. Sanderson, C.S. Punshon and J.D. Russell, Advanced Welding Processes for Fusion Reactor Fabrication, *Fusion Eng. Des.*, 2000, **49–50**, p 77–87.
13. A. Chamanfar, M. Jahazi, A. Bonakdar, E. Morin and A. Firoozrai, Cracking in Fusion Zone and Heat Affected Zone of Electron Beam Welded Inconel-713LC Gas Turbine Blades, *Mater. Sci. Eng. A.*, 2015, **642**, p 230–240.
14. M.H. Khani Sanij, S.S. Ghasemi Banadkouki, A.R. Mashreghi and M. Moshrefifar, The Effect of Single and Double Quenching and Tempering Heat Treatments on the Microstructure and Mechanical Properties of AISI 4140 Steel, *Mater. Des.*, 2012, **42**, p 339–346.
15. A.H. Meysami, R. Ghasemzadeh, H. Seyedyn, M.R. Aboutalebi and R. Rezaei, The Microstructure and Mechanical Properties of Direct-Quenched and Tempered AISI 4140 Steel, *TMS Annual Meeting.*, 2011, **2**, p 745–753.
16. X. You, Y. Tan, H. Cui, H. Zhang, X. Zhuang, L. Zhao, S. Niu, Y. Li and P. Li, Microstructure Evolution of an Inconel 713LC Alloy Prepared by Electron Beam Smelting, *Mater. Charact.*, 2021, **173**, p 110925.
17. J.T. Tharappel and J. Babu, Welding Processes for Inconel 713LC-A Brief Review, *IOP Conf. Ser. Mater. Sci. Eng.*, 2018, **330**, p 012082.
18. Y. Danis, C. Arvieu, E. Lacoste, T. Larrouy and J.M. Quenisset, An Investigation on Thermal, Metallurgical and Mechanical States in Weld Cracking of Inconel 738LC Superalloy, *Mater. Des.*, 2010, **31**, p 402–416.
19. O.A. Ojo, N.L. Richards and M.C. Chaturvedi, Contribution of Constitutional Liquation of Gamma Prime Precipitate to Weld HAZ Cracking of Cast Inconel 738 Superalloy, *Scr. Mater.*, 2004, **50**, p 641–646.
20. H. Ramezani and S. Mousavi, Characterization of Micro Structural and Mechanical Properties of Inconel 625/A 517 High Strength Quenched and Tempered Steel Dissimilar Welds, *Modares Mech. Eng.*, 2015, **14**, p 331–336.
21. O.A. Ojo and M.C. Chaturvedi, On the Role of Liquated γ' Precipitates in Weld Heat Affected Zone Microfissuring of a Nickel-Based Superalloy, *Mater. Sci. Eng. A.*, 2005, **403**, p 77–86.
22. A. Mirak, B. Shams and S. Bakhshi, Dissimilar Welding of Inconel 713 Superalloy and AISI 4140 Steel Using Nd:YAG Pulse Laser: An Investigation on the Microstructure and Mechanical Properties, *Opt. Laser Technol.*, 2022, **152**, p 108143.
23. X.B. Liu, M. Pang, Z.G. Zhang, W. Ning, C.Y. Zheng and G. Yu, Characteristics of Deep Penetration Laser Welding of Dissimilar Metal Ni-Based Cast Superalloy K418 and Alloy Steel 42CrMo, *Opt. Lasers Eng.*, 2007, **45**, p 929–934.
24. M. Sabzi and S.M. Dezfuli, Drastic Improvement in Mechanical Properties and Weldability of 316L Stainless Steel Weld Joints by Using Electromagnetic Vibration During GTAW Process, *J. Manuf. Process.*, 2018, **33**, p 74–85.
25. M. Sabzi, S.H. Mousavi Anijdan, A.R.B. Chalandar, N. Park, H.R. Jafarian and A.R. Eivani, An Experimental Investigation on the Effect of Gas Tungsten Arc Welding Current Modes Upon the Microstructure, Mechanical, and Fractography Properties of Welded Joints of Two Grades of AISI 316L and AISI310S Alloy Metal Sheets, *Mater. Sci. Eng. A.*, 2022, **840**, p 142877.
26. M. Sabzi and S.M. Dezfuli, Post Weld Heat Treatment of Hypereutectoid Hadfield Steel: Characterization and Control of Microstructure, Phase Equilibrium, Mechanical Properties and Fracture Mode of Welding Joint, *J. Manuf. Process.*, 2018, **34**, p 313–328.
27. K.D. Ramkumar, R. Ramanand, A. Ameer, K.A. Simon and N. Arivazhagan, Effect of Post Weld Heat Treatment on the Microstructure and Tensile Properties of Activated Flux TIG Welds of Inconel X750, *Mater. Sci. Eng. A.*, 2016, **658**, p 326–338.
28. L. Guo, F. Xiao, F. Wang, Z. Wei and Y. Zhang, Effect of Post-Weld Heat Treatment Temperatures on Microstructure, Intergranular Corrosion Resistance, and Mechanical Properties of 4130 Steel with Inconel 625 Weld Overlay, *J. Fail. Anal. Prev.*, 2021, **21**, p 1775–1783.
29. A.S.T.M. International. ASTM G5-94: Standard Reference Test Method For Making Potentiostatic and Potentiodynamic Anodic Polarization Measurements, ASTM International, West Conshohocken, PA, USA
30. M. Fisk, J. Andersson, R. du Rietz, S. Haas and S. Hall, Precipitate Evolution in the Early Stages of Ageing in Inconel 713LC Investigated using Small-Angle X-Ray Scattering, *Mater. Sci. Eng. A.*, 2014, **612**, p 202–207.
31. C. Slama and M. Abdellaoui, Structural Characterization of the Aged Inconel 713LC, *J. Alloys Compd.*, 2000, **306**, p 277–284.

Publisher's Note Springer Nature remains neutral with regard to jurisdictional claims in published maps and institutional affiliations.

Springer Nature or its licensor (e.g. a society or other partner) holds exclusive rights to this article under a publishing agreement with the author(s) or other rightsholder(s); author self-archiving of the accepted manuscript version of this article is solely governed by the terms of such publishing agreement and applicable law.